Oxidation effect on the shear strength of graphene on aluminum and titanium surfaces

Soumendu Bagchi,[1] Changhong Ke,[2] and Huck Beng Chew[1,*]
[1]*Department of Aerospace Engineering, University of Illinois at Urbana-Champaign, Urbana, Illinois 61801, USA*
[2]*Department of Mechanical Engineering and Materials Science and Engineering Program, State University of New York at Binghamton, Binghamton, New York 13902, USA*

(Received 26 July 2018; revised manuscript received 27 September 2018; published 13 November 2018)

We report the interfacial shear strength of graphene on pure and oxidized Ti and Al metal surfaces using density functional theory calculations. Our results show significant changes to the graphene-metal bonding properties in the presence of an oxide phase. In particular, the strongly chemisorbed interface between graphene and pure Ti is drastically weakened by the formation of a metal-oxide phase, while the weakly physisorbed interface between graphene and pure Al is significantly strengthened through the metal oxide formation. These oxidation effects can be modulated to some extent by the presence of vacancy or Stone-Wales defects which increases the binding interactions of weaker graphene-metal interfaces. These dramatic changes to the interfacial properties by surface oxidation explain the results of recent carbon nanotube pull-out experiments from Al and Ti metal-matrix nanocomposites.

DOI: 10.1103/PhysRevB.98.174106

I. INTRODUCTION

Graphene is a single atomic sheet of carbon atoms that has exceptional mechanical, thermal, and electrical properties [1,2]. There has been considerable interest in using graphene or its rolled counterpart, carbon nanotube (CNT), as a reinforcement in metal-matrix composites (MMCs) [3–5] because of their inherent stability at elevated temperatures, high stiffness and strength, as well as superior electrical and thermal conductivity derived from the metal matrices. Such unique combination of properties relies on effective bonding along the graphene-metal interface [6,7]. First-principles calculations show that some metals, such as Ni(111), Ti(0001), and Ru(0001) [6,8–10], undergo strong binding with graphene through chemisorption, while other metals, such as Al(111), Pt(111), and Ir(111) [8,9,11,12], exhibit weak interactions through physisorption. Despite the predicted strong graphene-Ti binding interactions, the mechanical properties of CNT-reinforced Ti-MMCs have fallen short of anticipated levels. For example, the addition of ∼0.4 wt. % of CNTs in Ti-MMCs increases the ultimate tensile strength of Ti by ∼11–28% to ∼754 MPa [13,14], which is still lower than the ∼900 MPa tensile strength of commercially available Ti-6Al-4V alloys [15]. Failure of these composites in the form of nanotube pull-out suggests a lack of effective load transfer between the nanotube and the metal matrix [4]. Contrary to the purported weak Al-graphene versus strong Ti-graphene binding, single-nanotube pull-out studies from Ti- and Al-MMCs further showed that the pull-out loads for CNT-Ti were only ∼32% higher than for CNT-Al, and the trend was reversed for thermally annealed MMCs [16].

The interfacial load transfer mechanisms in nanocomposite structures are sensitive to reaction products formed along the high density of interfaces [17]. Pristine graphene is generally inert and does not react with its host metal. The metal surface, by contrast, is reactive and forms oxides at elevated processing temperatures, under thermal annealing conditions, or even when exposed to the ambient environment. The binding properties of graphene on surface-oxidized metals can differ profoundly from those on bare metals. Here, we conduct first-principles calculations to quantify the barrier energy and shear strength for sliding of graphene on pure and oxidized Al and Ti surfaces. We demonstrate that surface oxidation lowers (increases) the interfacial shear strength (IFSS) of graphene on Ti (Al) by two orders of magnitude. These dramatic changes to the interfacial properties explain the results of single-nanotube pull-out experiments [16,18] from Al and Ti-MMCs prior to and after thermal annealing.

II. MODELING

We model monolayer graphene on (a) bare metal surfaces of Al(111) and Ti(0001), (b) monolayer O atoms bonded to the exposed Al(111) and Ti(0001) metal surfaces at the stable fcc absorption sites [19–21], and (c) O-terminated bulk α-Al_2O_3(0001) and rutile TiO_2 (110), as shown in Fig. 1(a). These respective graphene-metal systems depict increasing extents of oxidation, which transform the substrate from its bare metal form (Ti, Al), to having a mono layer of oxide on the surface (Ti-O, Al-O), and finally allowing subsurface diffusion of O atoms to form thick bulk oxide interphases of the respective metals (TiO_2, Al_2O_3). We model 2×2 unit cells of graphene below the metal lattice for each supercell, with exception of TiO_2-graphene where we model larger 6×6 unit cells of graphene because of the larger mismatch in lattice parameters between graphene and TiO_2(110). The resulting average in-plane lattice-mismatch strains are 1.1% for (Al, Al-O)-graphene, 4.3% for (Ti, Ti-O)-graphene, 2.9% for Al_2O_3-graphene, and 1.9% for TiO_2-graphene. We introduce a

*Corresponding author: hbchew@illinois.edu

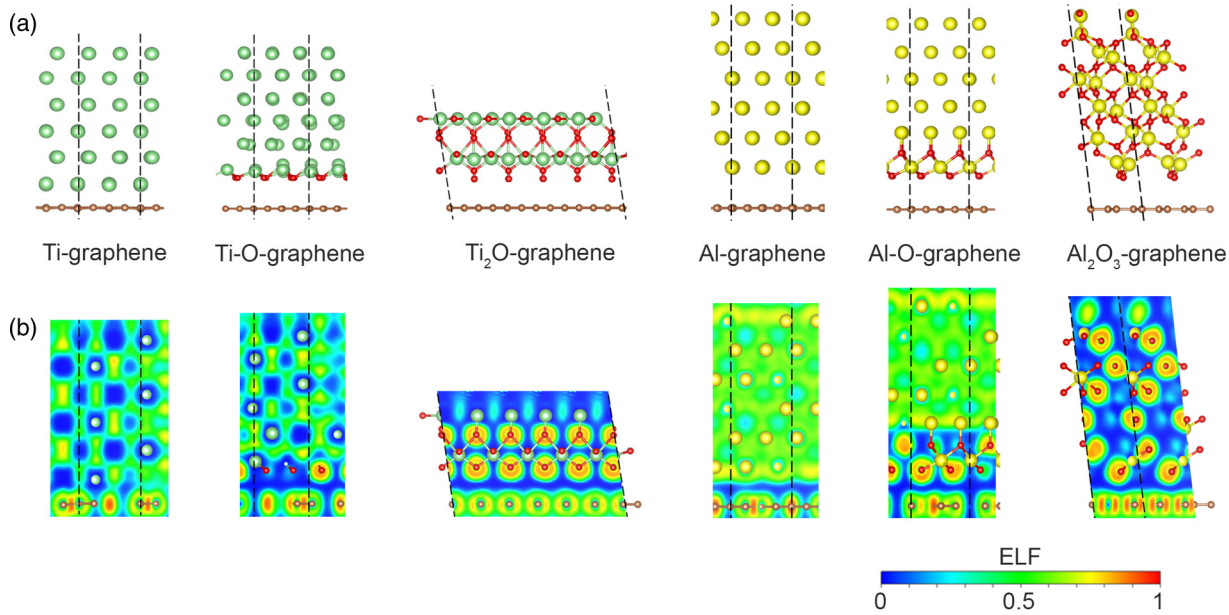

FIG. 1. Cross-sectional views of the (a) atomic configurations and (b) electron-localized function (ELF) contours of graphene on bare metal surfaces of Al (Al-graphene) and Ti (Ti-graphene), O atoms bonded to exposed Al (Al-O-graphene) and Ti (Ti-O-graphene) metal surfaces, and O-terminated bulk α-Al_2O_3 (Al_2O_3-graphene) and rutile TiO_2 (TiO_2-graphene). Atoms colored in red, green, yellow, and orange represent O, Ti, Al, and C, respectively. Dashed black lines denote in-plane periodicity of the supercells. An ELF contour value of close to 0.5 (green) corresponds to a uniform smeared-out electron cloud as in metallic bonding, while an ELF value of 1.0 (red) denotes high probability of finding electron localization as in covalent bonding.

10–12 Å vacuum layer above the top free surface of the metal or metal-oxide substrate to avoid interactions of the periodic images. Throughout our simulations, we freeze the top three rows of atoms (two in the case of TiO_2) in their bulk lattice positions to represent that of the bulk metal or metal-oxide substrate.

Our density functional theory (DFT) calculations are performed using VASP [22–24]. The projector augmented wave based pseudopotentials [24,25] are used to represent the interaction between ionic cores and valence electrons, while the Ceperley-Alder form of the local density approximation [26] as parametrized by Perdew and Zunger is adopted for exchange and correlation [27]. Gamma centered $5 \times 5 \times 1$ Monkhorst-Pack k-point grids are used for Brillouin-zone sampling in all the above pristine graphene-metal systems, except for TiO_2-graphene where the larger in-plane dimensions of the supercell permitted the use of a smaller $2 \times 2 \times 1$ k-point sampling. Throughout our simulations, we adopt an electronic kinetic-energy cutoff of 450 eV for the plane-wave basis sets describing valence electrons.

III. RESULTS

Previous studies have used the equilibrium interfacial binding distance of $2.0 < d < 2.5$ Å to denote chemisorption due to strong interactions, and $d > 3.0$ Å to denote physisorption associated with weak interactions [28]. Based on this simple criterion, our DFT calculations for the respective structures after quantum-mechanical relaxation [Fig. 1(a)] show that graphene is chemisorbed on Ti(0001) with $d = 2.16$ Å, but is physisorbed on Ti-O with $d = 3.00$ Å and weakly chemisorbed on TiO_2 with $d = 2.66$ Å. In contrast, graphene is physisorbed on Al(111) with $d = 3.16$ Å, but the interaction transitions to weak chemisorption with $d = 2.95$ and 2.60 Å on Al-O and Al_2O_3, respectively. These trends are also reflected in the electron localized function (ELF) contours for all three graphene-metal systems [Fig. 1(b)], which depict the probability of finding an electron near another electron with the same spin. We observe distinctly higher ELF values of ~0.3 across Ti-graphene versus ~0.1 across Al-graphene, because of hybridization of the unoccupied d orbitals in transition Ti metal with the $2p$ orbitals of C atoms in graphene [9,29]. For graphene on Ti-O and Al-O substrates, or on bulk TiO_2 and Al_2O_3 phases, the Ti-C and Al-C interactions are weakened by O atoms on the metal surface which reside above the graphene π cloud. Instead, the graphene-metal binding properties are primarily due to polarizing effects of the electronegative O atoms interacting with the π orbitals of graphene C atoms across the interface [30]. See the localization of electron pockets in the vicinity of the O atoms closest to the graphene sheet for both oxides of Ti and Al in Fig. 1(b). Close examination of the ELF contours for TiO_2-graphene versus Al_2O_3-graphene in the vicinity of the O-terminated interface shows higher electron densities (higher ELF intensities) for the latter, which suggests stronger localized bonding between graphene and Al_2O_3 as compared to graphene and TiO_2.

We quantify the barrier energies and barrier strengths for graphene-metal interfacial sliding by reconstructing the entire potential-energy landscape to find possible minimum-energy pathways for interfacial sliding. Figures 2(a) and 3(a) show

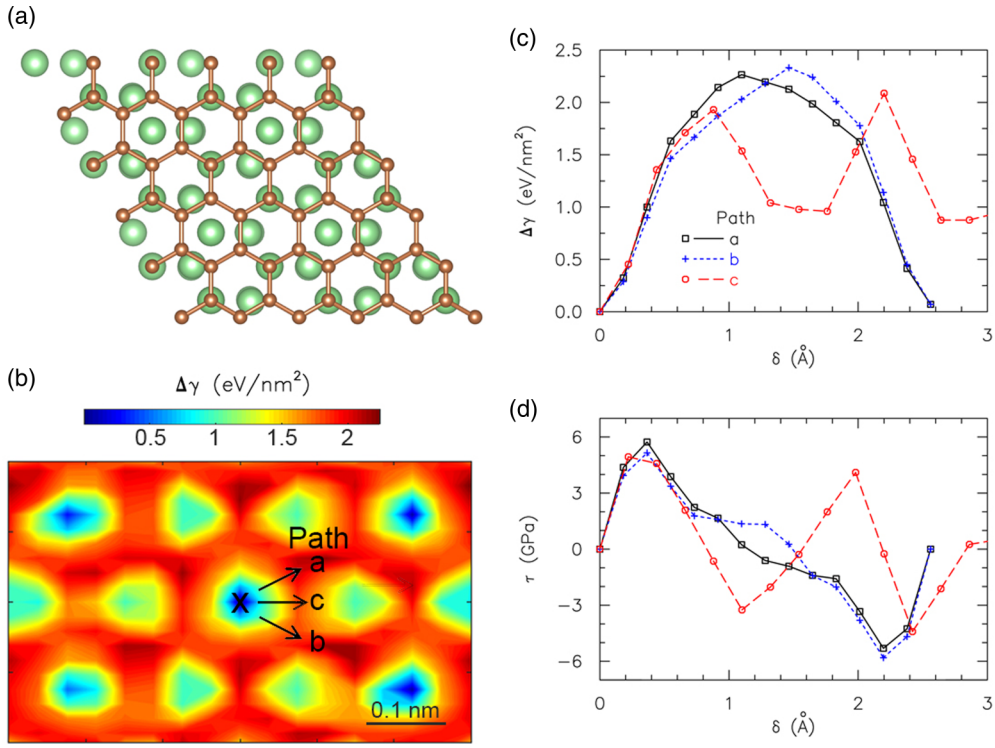

FIG. 2. Sliding of graphene on the bare Ti surface. (a) In-plane atomic configuration of Ti-graphene at the initial minimum-energy state, as viewed from the bottom. (b) Energy contours $\Delta\gamma$ associated with in-plane sliding of graphene for Ti-graphene. (c,d) Evolution of $\Delta\gamma$ and shear stress τ along possible minimum-energy sliding pathways a–c marked in (b).

the in-plane atomic configurations for Ti- and Al-graphene at the initial minimum-energy state ($\Delta\gamma = 0$), as viewed from the bottom. We iteratively displace the graphene layer with respect to the metal substrate at ∼0.5 Å intervals in the horizontal and lateral in-plane directions. After each translational displacement, we fix the in-plane positions of the ions while allowing them to relax in the out-of-plane directions, and calculate the change in energy, $\Delta\gamma$, normalized with respect to the interfacial area. The energy tolerance for ionic relaxation through the conjugate gradient method ranges from 10^{-4} to 10^{-7} eV depending on the calculated $\Delta\gamma$ for the various graphene-metal interfaces. Figures 2(b) and 3(b) show the energy contours $\Delta\gamma$ associated with in-plane sliding of graphene on bare Ti and Al; the symbol "x" denotes the initial state, while a sample of possible minimum-energy pathways for interfacial sliding is marked by arrows. Each pathway a–c connects the initial state to a second local minimum-energy state, represented by a stable energy well (blue), and we show the evolution of $\Delta\gamma$ along each of these sliding pathways in Figs. 2(c) and 3(c). The corresponding shear stress along the sliding pathways, $\tau = \frac{d\Delta\gamma}{d\delta}$, is shown in Figs. 2(d) and 3(d). For Ti-graphene, pathways a and b have nearly identical ($\Delta\gamma$, τ) versus δ profiles because of symmetry, with barrier energies of ∼2.3 eV/nm^2 and critical shear strengths of ∼5.5 GPa for interfacial sliding; pathway c has marginally lower barrier energy of ∼2.0 eV/nm^2 and critical shear strength of ∼5 GPa. These high barrier energies and critical shear strengths for sliding of graphene on bare Ti are a direct result of strong interfacial interactions due to chemisorption. In comparison, the weak physisorption interactions between graphene and bare Al allow for interfacial sliding with negligible barrier energies of ∼2.6–3.1 × 10^{-3} eV/nm^2 and low critical strengths of ∼1.0–1.1 × 10^{-2} GPa.

Figure 4(a) shows the in-plane atomic configurations of graphene on oxidized Ti and Al surfaces at the initial minimum-energy state, i.e., $\Delta\gamma = 0$. The corresponding $\Delta\gamma$ energy contours for interfacial sliding are shown in Fig. 4(b). Observe that the $\Delta\gamma$ contour for Al-O-graphene preserves the threefold symmetry of Al-graphene, as also shown by the near-identical $\Delta\gamma$ and τ profiles along the three sliding pathways a–c [Figs. 5(c) and 6(c)], which allows for isotropic interfacial slip. The formation of a bulk Al_2O_3 phase, however, creates a distinct lower-energy sliding direction along path a. This preferred sliding path (path a) has a 2.5-fold lower barrier energy [Fig. 5(d)] and 1.8-fold lower critical shear strength [Fig. 6(d)] compared to the next-lowest-energy pathway (path b), which results in anisotropic slip. The threefold symmetry in the $\Delta\gamma$ contours, indicative of isotropic slip, is somewhat loosely maintained for both Ti-O- and TiO_2-graphene [Figs. 5(a), 5(b), 6(a), and 6(b)].

We summarize the average critical barrier energy $\Delta\gamma^c$ and average critical shear strength τ^c for graphene sliding along the low-energy pathways of the various substrates in Table I, and include the maximum deviation to denote the extent of anisotropic slip. Observe that the formation of a monolayer of oxide on the surface of Ti decreases both $\Delta\gamma^c$ and τ^c from a high 2.23 eV/nm^2 and 5.27 GPa to 0.039 eV/nm^2 and

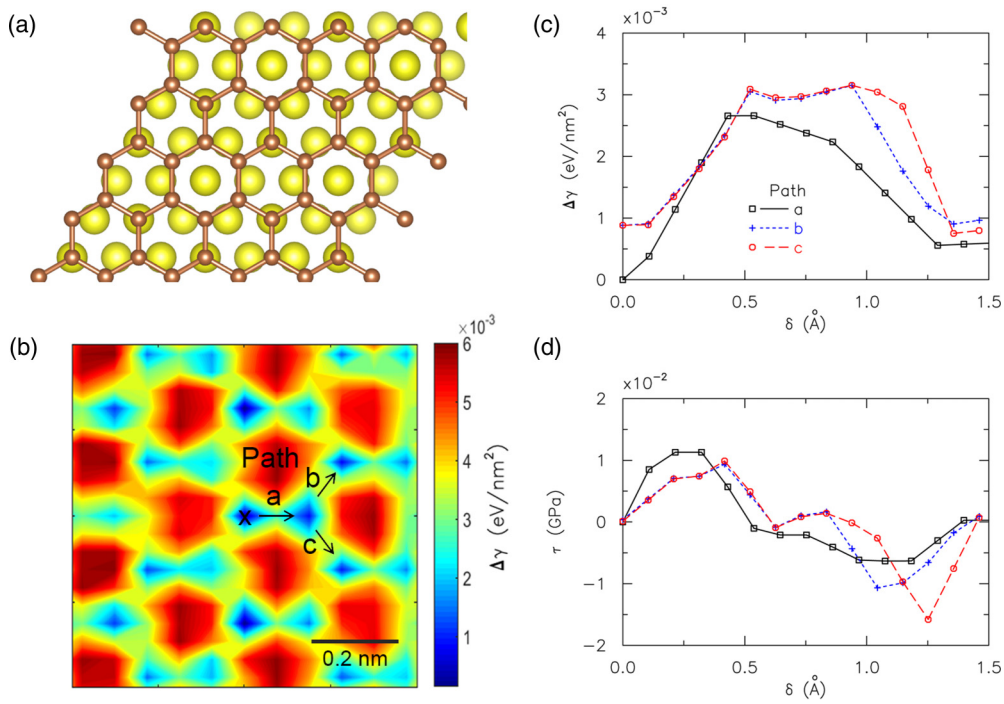

FIG. 3. Sliding of graphene on the bare Al surface. (a) In-plane atomic configuration of Al-graphene at the initial minimum-energy state, as viewed from the bottom. (b) Energy contours $\Delta\gamma$ associated with in-plane sliding of graphene for Al-graphene. (c, d) Evolution of $\Delta\gamma$ and shear stress τ with sliding displacements δ along possible minimum-energy pathways a–c marked in (b).

0.07 GPa. The formation of thicker bulk TiO_2 oxide phases further decreases $\Delta\gamma^c$ and τ^c threefold to $0.013\,\mathrm{eV/nm^2}$ and 0.02 GPa, respectively. In comparison, the weak physisorption interaction for Al-graphene results in negligible $\Delta\gamma^c$ and τ^c of $0.003\,\mathrm{eV/nm^2}$ and 0.01 GPa, respectively. While the formation of a monolayer of oxide on the surface of Al(111)

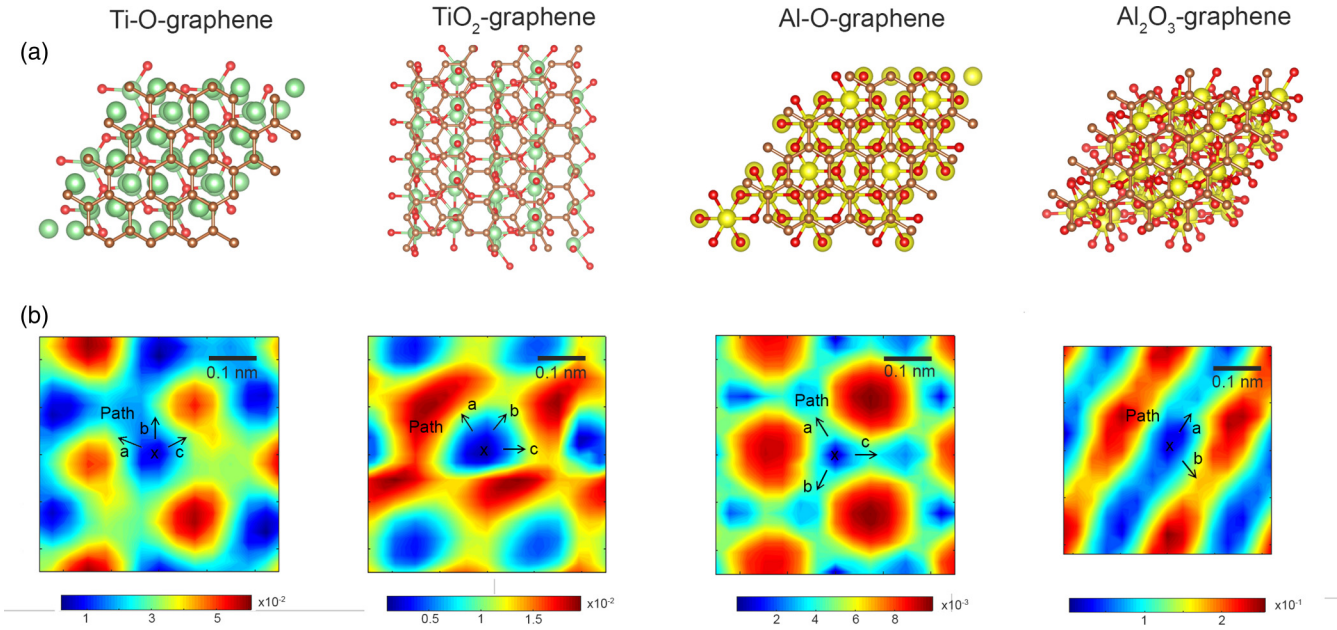

FIG. 4. Sliding of graphene on oxidized Ti and Al. (a) In-plane atomic configurations of graphene on surface-oxidized (Ti-O, Al-O) and bulk oxide (TiO_2, Al_2O_3) metals, as viewed from the bottom. (b) Energy contours $\Delta\gamma$ associated with in-plane sliding of graphene on the respective metal substrates.

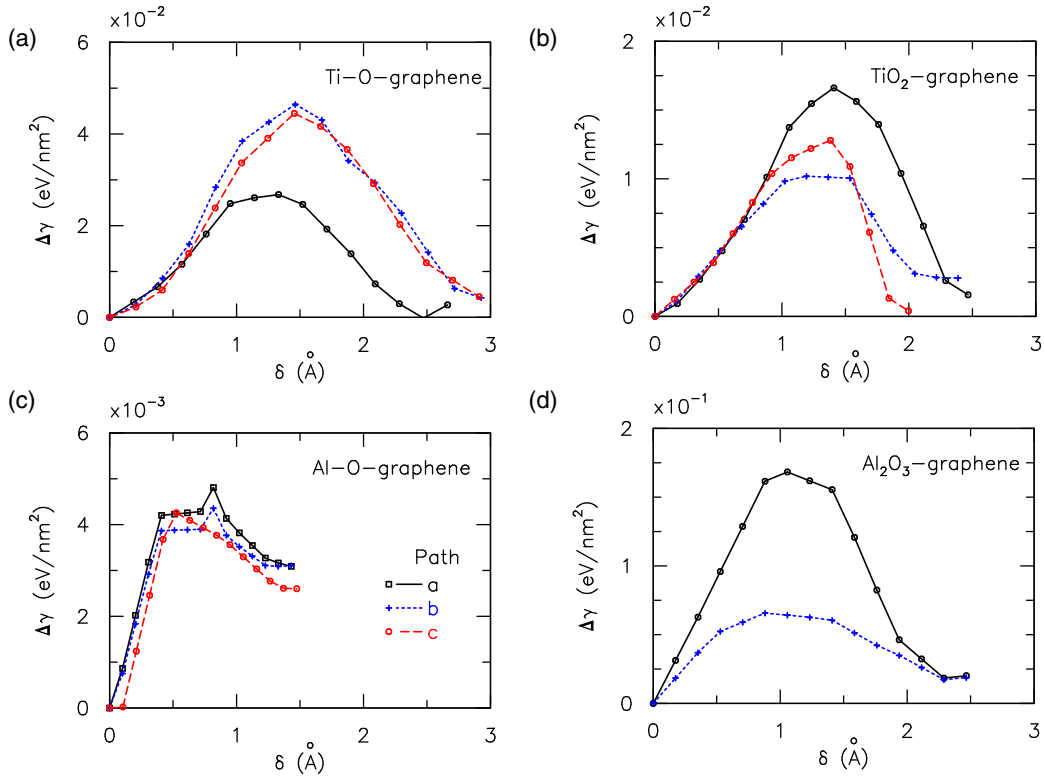

FIG. 5. Evolution of energy change $\Delta\gamma$ vs sliding displacement δ of graphene along possible minimum-energy sliding pathways of (a) Ti-O, (b) TiO_2, (c) Al-O, and (d) Al_2O_3 substrates.

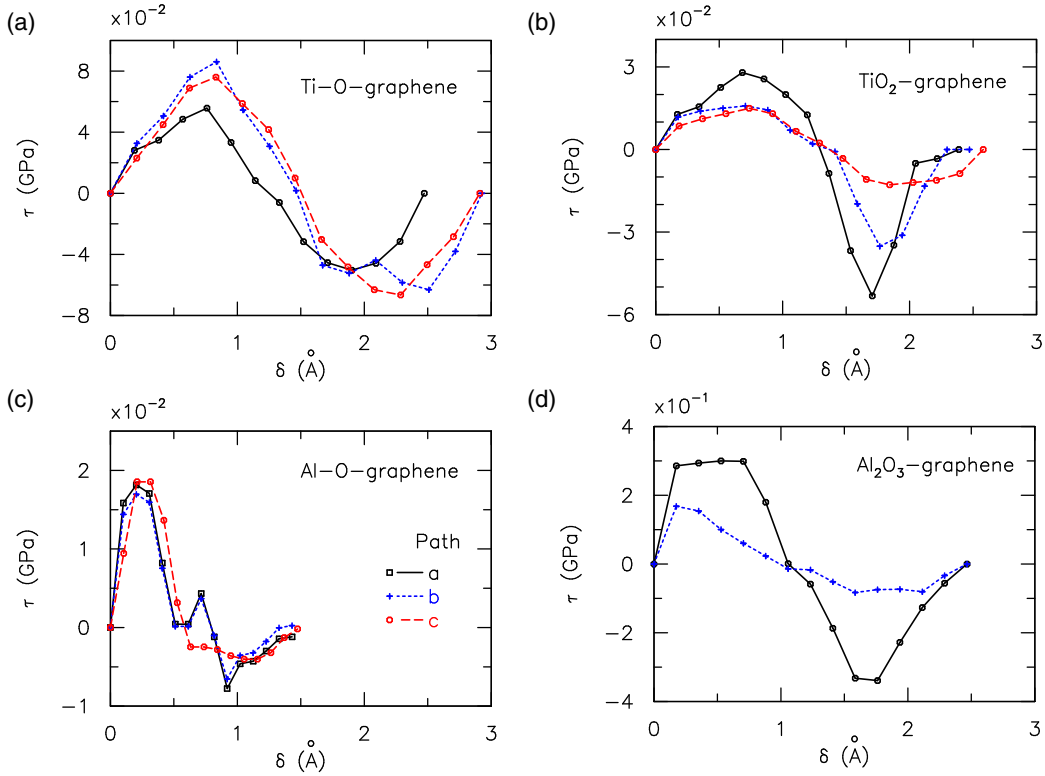

FIG. 6. Evolution of shear stress τ vs sliding displacement δ of graphene along possible minimum-energy sliding pathways of (a) Ti-O, (b) TiO_2, (c) Al-O, and (d) Al_2O_3 substrates.

TABLE I. Summary of binding energy E_b, as well as barrier energy $\Delta\gamma^c$ and critical shear strength τ^c for interfacial sliding of graphene on surfaces of bare metal Ti and Al, surface-oxidized Ti and Al, and bulk Ti and Al oxides.

Structure	Graphene-lattice defects	E_b(eV/nm^2)	$\Delta\gamma^c$(eV/nm^2)	τ^c (GPa)
Ti-graphene	Pristine	15.8	2.23 ± 0.14	5.27 ± 0.46
	Stone-Wales	17.1	1.71 ± 0.15	3.95 ± 0.47
	Vacancy	18.7	1.88 ± 0.019	5.78 ± 0.16
Ti-O-graphene	Pristine	0.85	0.039 ± 0.011	0.07 ± 0.015
TiO_2-graphene	Pristine	3.62	0.013 ± 0.003	0.02 ± 0.012
	Stone-Wales	3.82	0.286 ± 0.067	0.85 ± 0.020
	Vacancy	3.80	2.32 ± 0.43	5.19 ± 0.063
Al-graphene	Pristine	0.57	0.003 ± 0.0003	0.01 ± 0.001
	Stone-Wales	1.25	0.067 ± 0.009	0.13 ± 0.001
	Vacancy	2.26	0.69 ± 0.01	1.32 ± 0.28
Al-O-graphene	Pristine	2.21	0.004 ± 0.0003	0.02 ± 0.001
Al_2O_3-graphene	Pristine	3.68	0.117 ± 0.051	0.23 ± 0.066
	Stone-Wales	1.83	0.065 ± 0.007	0.13 ± 0.023
	Vacancy	2.83	0.10 ± 0.02	0.37 ± 0.07

does not significantly change $\Delta\gamma^c$ or τ^c, further oxidation to form a thicker bulk Al_2O_3 oxide phase creates a weakly chemisorbed interface with substantially larger $\Delta\gamma^c$ and τ^c of 0.117 eV/nm^2 and 0.23 GPa, respectively.

As grown graphene or CNTs from chemical vapor deposition (CVD) are rarely pristine, and may contain a small percentage of vacancy or Stone-Wales defects. Much higher defect densities can also be generated during transfer printing of CVD-grown graphene, or during sonication processes used to disperse and cut CNTs or graphene [31]. To quantify the contributions of these defects to the shear strength properties of graphene on bare Ti and Al metals and their TiO_2 and Al_2O_3 bulk oxide phases, we model larger 6×6 unit cells of graphene in the supercells of these four graphene-metal configurations, and introduce one 5-7-7-5 Stone-Wales defect (by rotating one C-C bond) or vacancy defect (by removing one C atom) in each graphene sheet. The larger 6×6 graphene sheet allows for increased separation distances between defects in the periodic simulation box ($2 \times 2 \times 1$ k-point sampling).

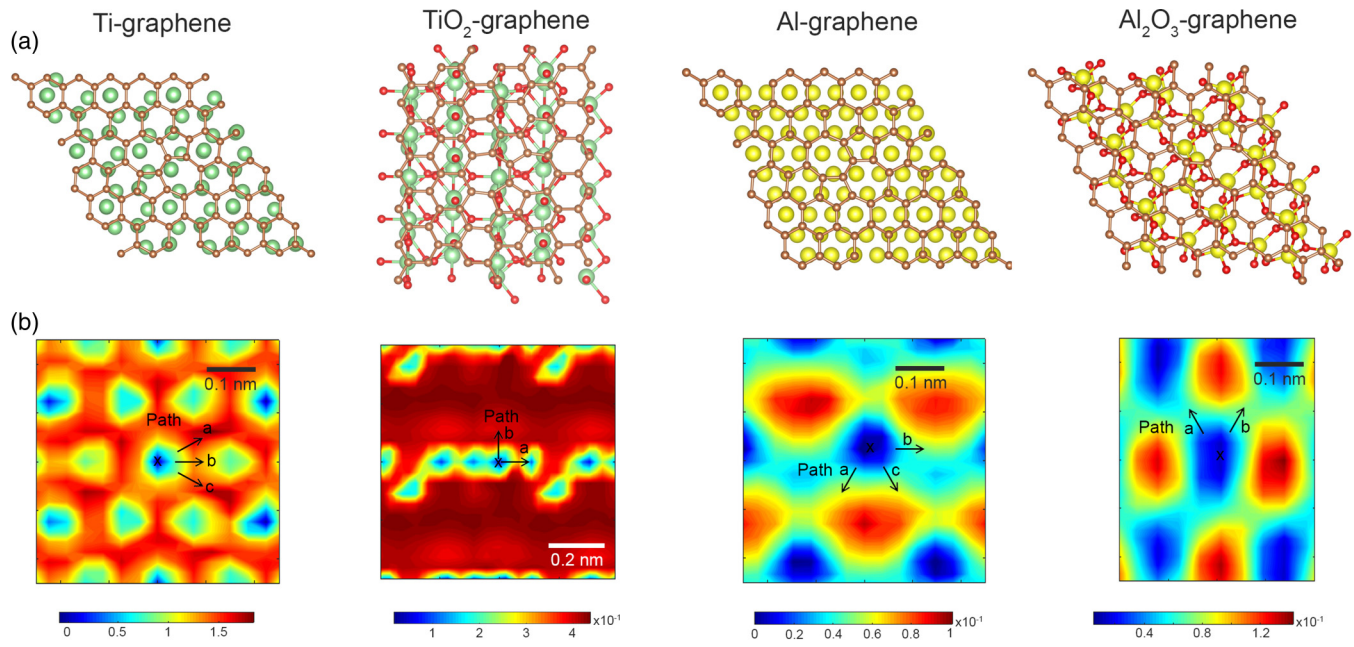

FIG. 7. Sliding of graphene with Stone-Wales defects on bare-metal Ti and Al surfaces and the respective bulk oxide surfaces. (a) In-plane atomic configurations of graphene on the respective metal substrates, as viewed from the bottom. (b) Energy contours $\Delta\gamma$ associated with in-plane sliding of graphene on the respective metal substrates.

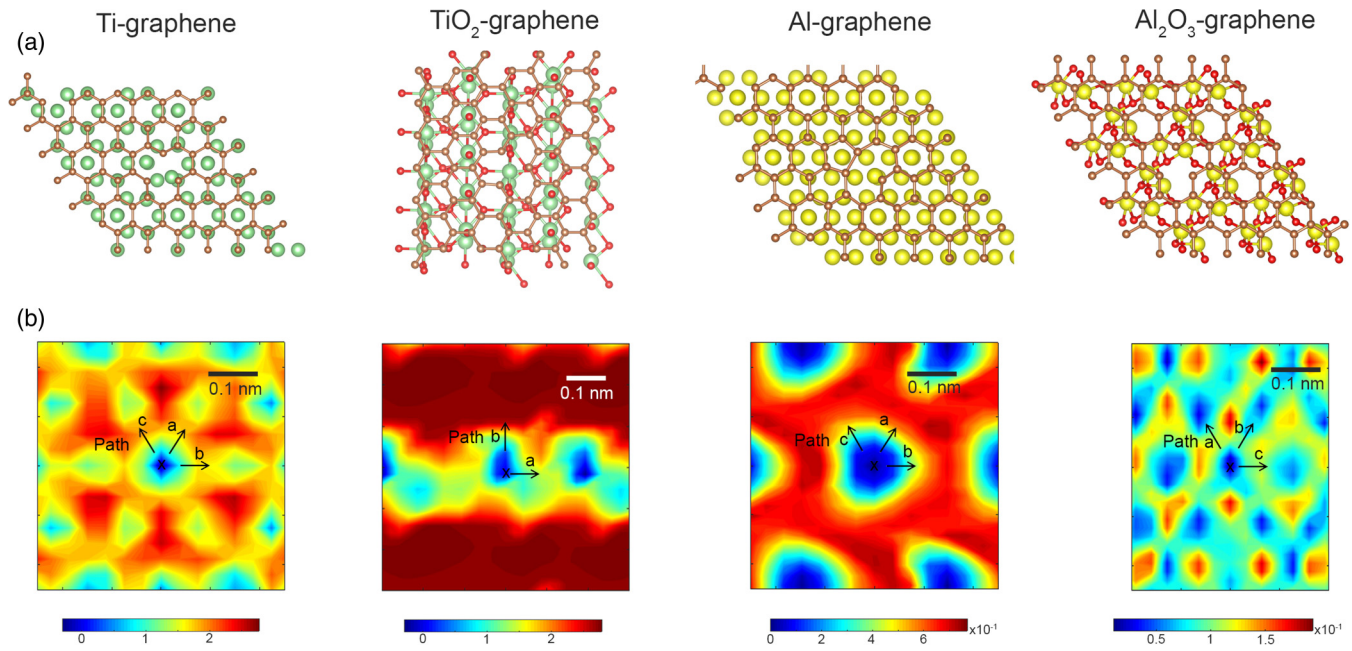

FIG. 8. Sliding of graphene with vacancy defects on bare-metal Ti and Al surfaces and the respective bulk oxide surfaces. (a) In-plane atomic configurations of graphene on the respective metal substrates, as viewed from the bottom. (b) Energy contours $\Delta\gamma$ associated with in-plane sliding of graphene on the respective metal substrates.

We reconstruct the $\Delta\gamma$ energy contour maps associated with graphene-metal sliding in the presence of Stone-Wales and vacancy defects (Figs. 7 and 8), and summarize the critical barrier energies $\Delta\gamma^c$ and shear strengths τ^c for interfacial sliding in Table I. We note that the $\Delta\gamma$ contours for Ti-graphene retain their threefold symmetry in the presence of Stone-Wales and vacancy defects; the associated $\Delta\gamma^c$ and τ^c are also not significantly different (<25%) in the presence of these defect types, implying that these lattice defects have limited contribution to the interfacial shearing properties presumably because of the already strong chemisorption interactions. For weaker TiO_2-graphene, however, Stone-Wales or vacancy defects tend to significantly increase τ^c by 4150% and 25 850% respectively; the $\Delta\gamma$ contours are also very different because of the deeper energy wells (blue) resulting from locally enhanced graphene-metal interactions at the defect site. These enhanced interactions result from changes in the local distribution of the π-electron density at the Stone-Wales defect site, or the formation of strong chemical bonds at the vacancy site [32,33]. Similar effects are observed for the weakly physisorbed Al-graphene, where locally enhanced Al-C bonding at the Stone-Wales or vacancy defect sites deepens the energy wells and increases both $\Delta\gamma^c$ and τ^c. In the case of stronger Al_2O_3-graphene interface, our results show no significant changes to $\Delta\gamma^c$ and τ^c in the presence of either Stone-Wales (∼44%) or vacancy defects (∼14% for $\Delta\gamma^c$ and ∼60% for τ^c), though a threefold symmetry in the $\Delta\gamma$ contours is recovered.

IV. DISCUSSIONS AND CONCLUSION

The binding energy, E_b, or work of adhesion is the energy required to separate the unit area of graphene from the metal surface and is widely used to quantify the graphene-metal binding interactions. This binding energy is related to, but different from, the calculated $\Delta\gamma^c$ for sliding of graphene on the metal surfaces. If E_b is smaller or comparable to $\Delta\gamma^c$, the graphene-metal interface readily separates to form a crack. If E_b is significantly larger than $\Delta\gamma^c$, interfacial sliding of graphene on the metal surface can occur without decohesion. Here, we calculate E_b from the difference between the relaxed energy of each graphene-metal system and that of the isolated metal substrate and free-standing graphene, per unit interfacial area. As shown in Table I, E_b dramatically decreases from 15.82 eV/nm^2 for Ti-graphene to 0.85 eV/nm^2 for Ti-O-graphene and 3.62 eV/nm^2 for TiO_2-graphene, but steadily increases from 0.57 eV/nm^2 for Al-graphene to 2.21 eV/nm^2 for Al-O-graphene and 3.68 eV/nm^2 for Al_2O_3-graphene. Note that the significantly lower E_b for Ti-O-graphene versus Al-O-graphene can be attributed to the twofold lower surface density of O atoms interacting with the π orbitals of graphene C atoms across the interface. For all six graphene-metal systems, the measured E_b values are consistently higher than $\Delta\gamma^c$ by several fold, which suggests shear-induced interfacial sliding to be the dominant failure mode.

Our DFT calculations demonstrate that oxidation dramatically reduces the binding interactions and shear strength properties of graphene on Ti, but significantly improves those of graphene on Al. These contrasting responses explain the results of prior experiments which conduct the pull-out of individual CNTs from Ti and Al matrices, which are summarized in Fig. 9. These experiments [16–18] report average IFSSs of 38 and 28 MPa for the pull-out of CNT along partially oxidized surfaces of Ti and Al matrices, respectively. Further oxidation of these matrices

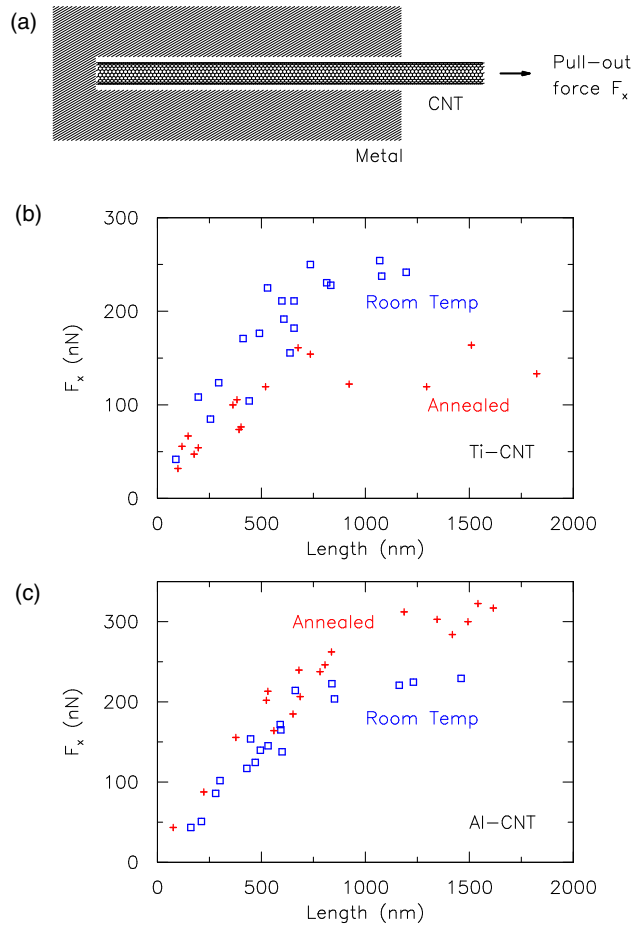

FIG. 9. Carbon nanotube (CNT) pull-out experiments from Ti and Al matrices. (a) Schematic of the pull-out process for a CNT with diameter of 3.12 nm subjected to applied pull-out force F_x. (b, c) Pull-out force vs nanotube length for Ti- and Al-CNT nanocomposites. Symbols in blue denote results from room-temperature experiments conducted without thermal annealing, while symbols in red denote results for thermally annealed nanocomposites. Results for thermally annealed Ti-CNT are currently unpublished, while the remaining results are published in [16,18].

by thermal annealing prior to CNT pull-out increased the average IFSS of CNT along Al to 35 MPa, but reduced that of graphene along Ti to 22 MPa. We remark that these experimental IFSS values are well within our DFT-calculated IFSS values of 20 to 230 MPa for graphene along surface-oxidized Al, and 20 to 70 MPa for graphene along surface-oxidized Ti.

In summary, we have quantified the shear-sliding resistance of graphene along both bare metal and oxidized Ti and Al surfaces. We found opposite changes to the sliding barrier energy and shear-strength properties of graphene on these two types of metals when surface oxidized: the high interfacial shear strength of ∼5 GPa along pure-Ti–graphene is reduced by two orders of magnitude to ∼20 MPa along TiO_2–graphene, while the interfacial shear strength of ∼10 MPa along pure-Al–graphene increases to ∼0.2 GPa along Al_2O_3–graphene. The presence of Stone-Wales or vacancy defects in graphene significantly improves the shear strength along weaker TiO_2–graphene and pure-Al–graphene interfaces, but has limited influence on stronger pure-Ti–graphene and Al_2O_3–graphene interfaces. These fundamental insights on graphene-metal interfaces have important implications for graphene-reinforced MMCs, fabrication of graphene-metal contacts in graphene transistors [34,35], as well as the transfer printing and epitaxial growth of graphene on metallic substrates [36,37].

ACKNOWLEDGMENTS

This work was supported by the NSF under Grants No. NSF-CMMI-1538162 (S.B. and H.B.C.) and No. NSF-CMMI-1537333 (C.H.K.), as well as the U.S. AFOSR Low Density Materials program under Grant No. FA9550-15-1-0491 (C.H.K.). We acknowledge the use of computational resources provided by the Blue Waters sustained-petascale computing project, which is supported by the NSF (Grants No. OCI-0725070 and No. ACI-1238993) and the state of Illinois, USA. Blue Waters is a joint effort of the University of Illinois at Urbana-Champaign and its National Center for Supercomputing Applications.

[1] A. K. Geim, Science **324**, 1530 (2009).
[2] R. M. Westervelt, Science **320**, 324 (2008).
[3] N. Y. Jin-Phillipp and M. Rühle, Phys. Rev. B **70**, 245421 (2004).
[4] B. Chen, J. Shen, X. Ye, L. Jia, S. Li, J. Umeda, M. Takahashi, and K. Kondoh, Acta Mater. **140**, 317 (2017).
[5] S. Feng, Q. Guo, Z. Li, G. Fan, Z. Li, D. B. Xiong, Y. Su, Z. Tan, J. Zhang, and D. Zhang, Acta Mater. **125**, 98 (2017).
[6] L. Adamska, Y. Lin, A. J. Ross, M. Batzill, and I. I. Oleynik, Phys. Rev. B **85**, 195443 (2012).
[7] T. Olsen and K. S. Thygesen, Phys. Rev. B **87**, 075111 (2013).
[8] D. Pacilé, P. Leicht, M. Papagno, P. M. Sheverdyaeva, P. Moras, C. Carbone, K. Krausert, L. Zielke, M. Fonin, Y. S. Dedkov, F. Mittendorfer, J. Doppler, A. Garhofer, and J. Redinger, Phys. Rev. B **87**, 035420 (2013).
[9] P. A. Khomyakov, G. Giovannetti, P. C. Rusu, G. Brocks, J. van den Brink, and P. J. Kelly, Phys. Rev. B **79**, 195425 (2009).
[10] X. Peng and R. Ahuja, Phys. Rev. B **82**, 045425 (2010).
[11] G. Giovannetti, P. A. Khomyakov, G. Brocks, V. M. Karpan, J. van den Brink, and P. J. Kelly, Phys. Rev. Lett. **101**, 026803 (2008).
[12] P. Sutter, J. T. Sadowski, and E. Sutter, Phys. Rev. B **80**, 245411 (2009).
[13] K. Kondoh, T. Threrujirapapong, H. Imai, J. Umeda, and B. Fugetsu, Compos. Sci. Technol. **69**, 1077 (2009).
[14] S. Li, B. Sun, H. Imai, T. Mimoto, and K. Kondoh, Compos. Part A: Appl. Sci. Manuf. **48**, 57 (2013).
[15] K. Firm, R. Boyer, and G. Welsch, *Materials Properties Handbook: Titanium Alloys* (ASM, Materials Park, Ohio, 1994).
[16] C. Yi, S. Bagchi, C. M. Dmuchowski, F. Gou, X. Chen, C. Park, H. B. Chew, and C. Ke, Carbon **132**, 548 (2018).

[17] W. Zhou, T. Yamaguchi, K. Kikuchi, N. Nomura, and A. Kawasaki, Acta Mater. **125**, 369 (2017).
[18] C. Yi, X. Chen, F. Gou, C. M. Dmuchowski, A. Sharma, C. Park, and C. Ke, Carbon **125**, 93 (2017).
[19] J. Liu, X. Fan, C. Sun, and W. Zhu, RSC Adv. **6**, 71311 (2016).
[20] M. Guiltat, M. Brut, S. Vizzini, and A. Hémeryck, Surf. Sci. **657**, 79 (2017).
[21] Y. Yourdshahyan, B. Razaznejad, and B. I. Lundqvist, Phys. Rev. B **65**, 075416 (2002).
[22] G. Kresse and J. Hafner, Phys. Rev. B **47**, 558 (1993).
[23] G. Kresse and J. Furthmüller, Phys. Rev. B **54**, 11169 (1996).
[24] G. Kresse and D. Joubert, Phys. Rev. B **59**, 1758 (1999).
[25] P. E. Blöchl, Phys. Rev. B **50**, 17953 (1994).
[26] D. M. Ceperley and B. J. Alder, Phys. Rev. Lett. **45**, 566 (1980).
[27] J. P. Perdew and A. Zunger, Phys. Rev. B **23**, 5048 (1981).
[28] J. Tao, H. Tang, A. Patra, P. Bhattarai, and J. P. Perdew, Phys. Rev. B **97**, 165403 (2018).
[29] A. L. Hsu, R. J. Koch, M. T. Ong, W. Fang, M. Hofmann, K. K. Kim, T. Seyller, M. S. Dresselhaus, E. J. Reed, J. Kong, and T. Palacios, ACS Nano **8**, 7704 (2014).
[30] S. Gowtham, R. H. Scheicher, R. Ahuja, R. Pandey, and S. P. Karna, Phys. Rev. B **76**, 033401 (2007).
[31] H. B. Chew, M. W. Moon, K. R. Lee, and K. S. Kim, Proc. R. Soc. A **467**, 1270 (2011).
[32] D. W. Boukhvalov and M. I. Katsnelson, Nano Lett. **8**, 4374 (2008).
[33] E. J. Duplock, M. Scheffler, and P. J. D. Lindan, Phys. Rev. Lett. **92**, 225502 (2004).
[34] M. Hasegawa and K. Nishidate, Phys. Rev. B **83**, 155435 (2011).
[35] F. Xia, V. Perebeinos, Y. M. Lin, Y. Wu, and P. Avouris, Nat. Nanotechnol. **6**, 179 (2011).
[36] H. Chen, W. Zhu, and Z. Zhang, Phys. Rev. Lett. **104**, 186101 (2010).
[37] A. Harpale, M. Panesi, and H. B. Chew, J. Chem. Phys. **143**, 104703 (2015).